Aminonaphthalic Anhydrides as Red-Emitting Materials: Electroluminescence, Crystal Structure, and Photophysical Properties

Aminul Islam, Ching-Chi Cheng, San-Hui Chi, Sheng Jui Lee, P. Gayatri Hela, I-Chia Chen,* and Chien-Hong Cheng*

Department of Chemistry, National Tsing Hua University, Hsinchu, Taiwan 30013, Republic of China

Received: November 22, 2004; In Final Form: January 25, 2005

The red and orange emitters (ANA-1−3) consisting of a 4-amino-1,8-naphthalic anhydride group were synthesized. The lowest absorption band of these ANA molecules centered at ≈450 nm is assigned to be a charge-transfer transition with emission at 514−536 nm in nonpolar solvents such as *n*-hexane and at ≈590−640 nm in polar solvents such as THF and CH_2Cl_2 and in the solid states. Emission lifetimes are measured with time-correlated single photon counting. Shorter lifetimes are observed for the ANA molecules when dissolved in polar solvents compared with those in nonpolar solvents. Strong dipole−dipole interaction of ANA molecules with solvents is indicated. At high concentrations the measured emission lifetimes, generally shortened from self-quenching, are found to remain about the same order of magnitude in ANAs. This implies that the exciton states of aggregates are formed and they exhibit a relatively long lifetime. Crystallographic data of 4-(phenyl antracen-9-yl) (ANA-2) and 4-(phenyl-2-naphthyl) amino-1,8-naphthalic anhydrides (ANA-3) show that the molecules exist as dimeric structures with antiparallel head-to-tail stacking of naphthalic anhydride planes in addition to other $\pi-\pi$ stacking. The strong dipole−dipole interactions and the $\pi-\pi$ stacking account for the observed red-shifted emissions of ANAs in the powders. For films prepared from vacuum sublimation, a structure similar to that in the crystal but with less crystalline order is expected based on the emission wavelength. Several electroluminescent devices based on these ANAs are reported here; they emit orange-red light at 602−628 nm with high brightness and steady external quantum efficiency.

1. Introduction

Tang and VanSlyke[1] were the first to employ vacuum deposition for the formation of thin-film organic light-emitting diodes (OLEDs). The great potential of OLED technologies in full-color displays has stimulated research in the development of new materials for high luminous efficiency, color purity, and durability. To date, a number of green and blue emitters with acceptable luminous efficiencies and reasonable color purity have been developed, while the short lifetime of blue emitters remains a concern.[2−6] Red emitters including pyran-containing compounds such as DCM1, DCM2,[7] DCJT, and DCJTB,[8] cyanine dyes,[9,10] porphyrin compounds,[11,12] europium chelates,[13] iridium complexes,[14] and other types of organic compounds[15] were reported. Most of these materials were used as dopants in the electroluminescent (EL) devices. In the continuing search for new red fluorescence materials for EL devices, we observed that 4-amino-1,8-naphthalic anhydride (ANA) derivatives, different from most of the fluorescence red emitters, can be used as direct red-light emitters in electroluminescent devices with good brightness. In addition, these molecules show interesting photophysical properties that vary with the environment. To the best of our knowledge, this class of compounds has not been tested as emitters for OLEDs, although several 1,8-naphthalic imides were employed with low efficiencies before.[17]

In this paper, we report the synthesis of this class of materials and the use of these organic compounds as direct red-light emitters in electroluminescent devices. In addition, to understand photophysical properties of emitting states of these molecules and their correlation to OLED thin films, we measure the fluorescent lifetimes and quantum yields in various solvents and in films. Quantum chemical calculations on one of the molecules are performed to study the structure and the characteristics of molecular orbitals involved in electronic excitation and to explain the observed spectral features. Two crystallographic structures are investigated to understand the crystal packing of these molecules in the solid state. From these studies we explain the large spectral shift of these derivatives in various solvents and in film and unravel the emission mechanism of these ANA molecules in EL devices.

2. Results

Synthesis of ANA Derivatives. The ANA derivatives ANA-1, ANA-2, and ANA-3 were successfully obtained from the reaction of 4-bromo-1,8-naphthalic anhydride with the corresponding secondary diarylamine in the presence of $Pd(OAc)_2$/$P(^tBu)_3$/NaO^tBu in *o*-xylene (Scheme 1).[16] All compounds are characterized by NMR and mass spectral data. For ANA-2 and -3, the structures were further confirmed by X-ray diffraction results. These ANA derivatives consist of a strongly electron-accepting anhydride group and a strongly electron-donating amino moiety along with a long conjugated system required for an intramolecular charge-transfer compound as red emitters.[7,8]

Photophysical Properties. The absorption and photoluminescent (PL) spectra of ANA-1−3 in *n*-hexane, benzene, tetrahydrofuran (THF), methylene chloride, and methanol are recorded to study their spectral properties under various solvent

* To whom correspondence should be addressed. E-mail: icchen@mx.nthu.edu.tw, chcheng@mx.nthu.edu.tw. Phone: +886-3-5715131 ext 3339. Fax: +886-3-5721614.

10.1021/jp044669u CCC: $30.25
Published on Web 03/04/2005

SCHEME 1: Synthetic Route for ANA Derivatives

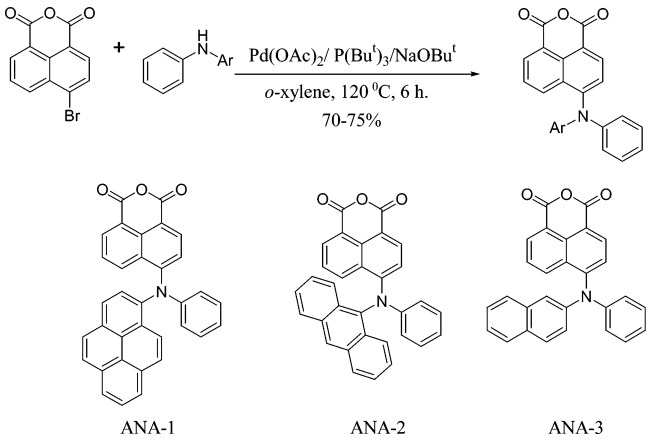

polarities and to compare their emission with those in films. The UV−vis absorption spectra are shown in Figure 1, while the normalized PL spectra of ANA-1 and ANA-2 in *n*-hexane and films and ANA-3 in *n*-hexane and benzene are presented in Figure 2a,b. As indicated in the absorption spectra, these derivatives reveal a common low-energy broad band at 400−500 nm assigned to an intramolecular charge-transfer band from the arylamino group to the naphthalic anhydride moiety (vide infra) in THF, benzene, and *n*-hexane. In contrast, a larger blue shift of ∼72 nm for ANA-1 and ANA-3 and ∼40 nm for ANA-2 for the low-energy absorption band were observed in methanol. The interaction of these molecules with methanol via hydrogen bonding likely accounts for this unusual behavior. It is noteworthy that the absorption maxima for the lowest energy band, λ_{max}^{abs} are close to each other and the variation is within 24 nm in all solvents except methanol used here, but the emission maxima, λ_{max}^{PL} vary to a much greater extent from 514−536 nm

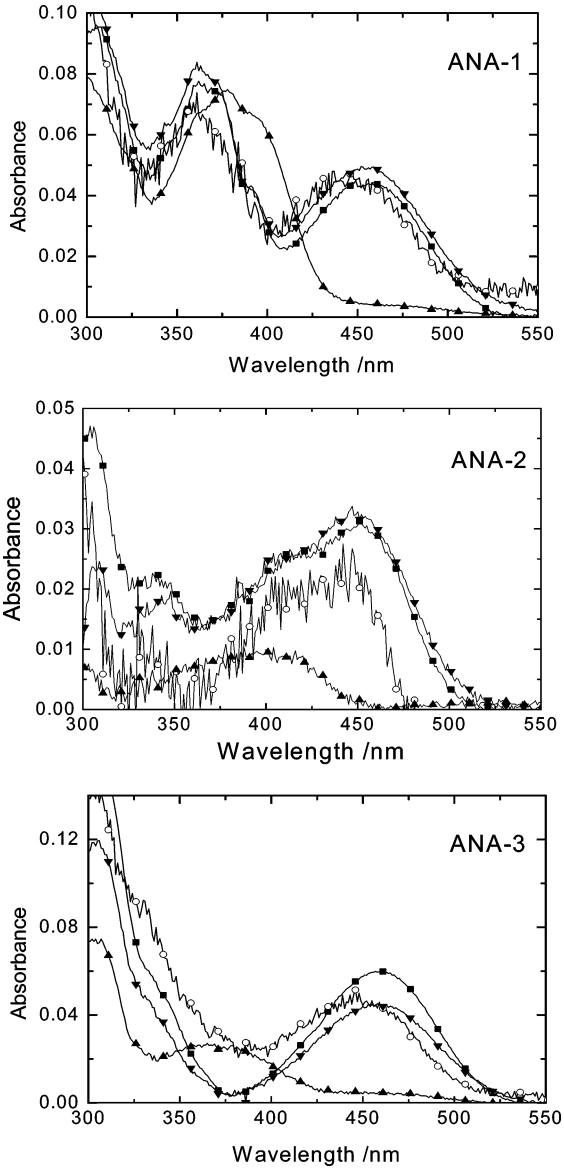

Figure 1. UV−vis absorption spectra of ANA-1, ANA-2, and ANA-3 in *n*-hexane (○, saturated solution), benzene (■, 3.8 × 10^{-6} M), THF (▼, 3.8 × 10^{-6} M), and methanol (▲, 3.8 × 10^{-6} M).

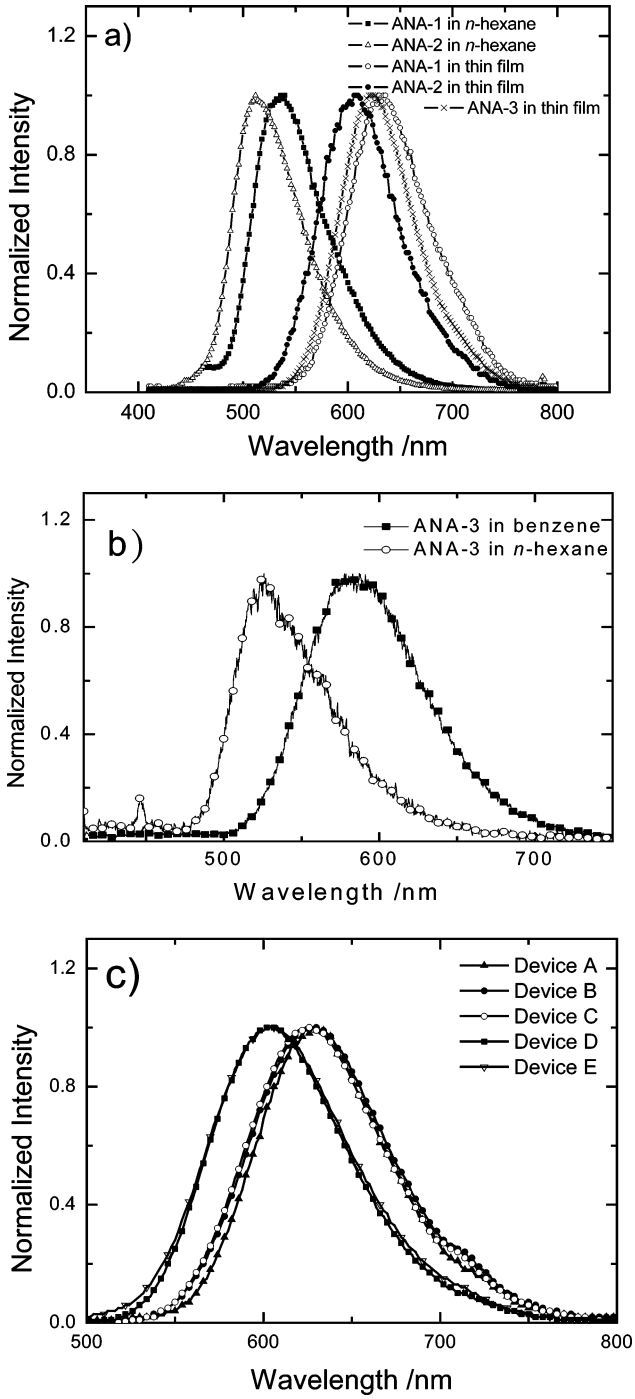

Figure 2. Normalized PL spectra of (a) ANA derivatives in *n*-hexane solution and the thin films of the derivatives prepared by vacuum deposition and (b) ANA-3 in *n*-hexane and in benzene; (c) normalized EL spectra of devices **A**−**E** at 7 V.

TABLE 1: UV−Vis and Photoluminescent Data, Melting and Glass Transition Points T_m and T_g, and Electrochemical Characteristics of ANA Derivatives

	λ_{max}^{abs} [a] (nm)				λ_{max}^{PL} [b] (nm)						λ_{max}^{EL}			HOMO	LUMO
compd	*n*-hexane	benzene	THF	CH_2Cl_2	*n*-hexane	benzene	THF	CH_2Cl_2	film	powder	(nm)	T_m (°C)	T_g (°C)	(eV)	(eV)
ANA-1	447	457	455	465	536	605	NA[c]	NA[c]	634	640	628	267	139	5.53	3.48
ANA-2	440	450	450	462	514	560	591	608	607	591	602	291	134	5.58	3.44
ANA-3	446	459	455	470	520	580	621	638	627	601	617	220	92	5.67	3.57

[a] Absorption maximum. [b] The excitation wavelength was at 393 nm, and films were prepared by vacuum deposition. [c] The letters NA represent that the data are not available.

TABLE 2: Emission Lifetimes Monitored at Various Wavelengths and Quantum Yields Measured in Solutions for ANA Derivatives[a]

	n-hexane			benzene		THF		film		
λ_{em} (nm)	530	580	600	600	600	600	600	580	600	700
concentration (M)	saturated soln	saturated soln	saturated soln	2.0×10^{-4}	6.3×10^{-6}	2.0×10^{-4}	6.3×10^{-6}			
				ANA-1						
τ (ns)	4.36	4.40	4.47	1.17	1.31			1.35	1.71	1.79
ϕ_f (%)	13.1			0.05	3.1					
				ANA-2						
τ (ns)	5.40	5.48	5.62	2.14	2.24	0.64	0.69	1.21	1.65	1.80
ϕ_f (%)	30.4			0.51	6.6	0.05	0.85			
				ANA-3						
τ (ns)	8.42	8.45	9.03	8.55	8.72	1.09	1.18	3.48	4.42	4.73
ϕ_f (%)	33.5			1.62	16.0	0.03	0.66			

[a] Emission from the lowest energy state with predominant excitation on the anhydride chromophore was integrated to obtain the quantum yields.

in *n*-hexane to 608−638 nm in CH_2Cl_2. The absorption and photoluminescent maxima of these ANA derivatives in various solvents and in film are summarized in Table 1. Both the absorption and emission of ANA-2 show consistent blue shifts from the other derivatives, although intuitively we expect ANA-3 with a naphthalene moiety should display the blue shifts. Other absorption bands in the low-wavelength region $\lambda < 400$ nm are assigned to the $\pi-\pi^*$ excitation of pyrenyl, anthracenyl, and naphthyl groups in ANA-1−3, respectively. For ANA-2, an additional absorption band appearing as a shoulder near 410 nm is assigned to be a $\pi-\pi^*$ transition occurring within the anthracenyl group.

In concentrated solutions, the shape of the intramolecular charge transfer low-energy absorption band remains unchanged but the pyrenyl and anthracenyl bands in ANA1 and ANA2, respectively, are red-shifted in high concentrations because of the formation of aggregates commonly known for arylenes.[18] For the charge-transfer band, the λ_{max}^{abs} of ANA-1−3 varies slightly, less than ±11 nm, as the concentration increases from 6×10^{-6} to 2×10^{-4} M. The greatest concentration is limited by ANA solubility. In *n*-hexane, these three ANA derivatives dissolve poorly so a saturated solution was used here to measure their photophysical properties. ANA-1 displays a fluorescence quantum yield $\phi_f = 13.1\%$ in *n*-hexane. The values increase to 30.4 and 33.5% for ANA-2 and ANA-3, respectively. The emission of these ANA derivatives in polar solvent THF is surprisingly weak probably due to efficient solvent quenching. For example, the emission of ANA-1 in THF is so weak that an attempt to record the PL spectrum failed. Table 2 lists the experimental fluorescence quantum yields ϕ_f of these compounds in various solvents and concentrations. As shown in the table, the low quantum yields at high concentrations are due to self-quenching. The lowest concentration of ANA derivatives used for the quantum yield measurement is ca. 6×10^{-6} M. Even at this concentration, self-quenching is still inevitable; hence ϕ_f reported here is the upper bound value. Overall the three derivatives show high fluorescence quantum yields in nonpolar solvents and the values decrease as the solvent polarity increases indicating strong quenching from dipole−dipole interaction of the solvent and the solute molecules.

As shown in Table 1, the emission maximum λ_{max}^{PL} of each ANA derivative varies dramatically with the solvent used and with the state. To further understand the nature of these fluorescent emissions, we correlate the variation to the solvent polarity using the Lippert equation:[19] $\nu_A = \nu_F + 2(\mu_e - \mu_g)^2 \Delta f / hca_o^3 + \text{const}$, in which μ_e and μ_g denote the dipole moment of the electronic excited and ground states, respectively, a_o is the radius of the cavity occupied by the solute molecule, and ν_A and ν_F are the frequencies of absorption and emission in wavenumbers, respectively. The derivation of this equation assumes a spherical fluorophore and the dipole vectors for the excited and ground states are similar. The Stokes shift $\nu_A - \nu_F$ is due to interactions of the fluorophore with its environment, i.e., solvent molecules. Parameter Δf denotes solvent polarity and is defined to be $(\epsilon - 1)/(2\epsilon + 1) - (n^2 - 1)/(2n^2 + 1)$; ϵ and n denote the static dielectric constant and the refractive index, respectively. Figure 3a shows the plot for the Stokes shift versus Δf. We also recorded the absorption and PL spectra for ANA-2 and ANA-3 in solvent CH_2Cl_2 because it is a polar solvent but does not involve in forming excitons with solute molecules. The strong dependence of the Stokes shift on Δf in Figure 3a indicates that the ANA derivatives are sensitive to their immediate environment. A larger Stokes shift is observed in polar solvents. In solvent THF and benzene, the shifts are above the straight line (shown in Figure 3a) and this may be due to the effect of interaction of the π-electron rich solvent with the π-electron system of the solute.[18c]

The PL lifetimes τ of these derivatives were measured for various solvents, concentrations, and emission wavelengths. Laser excitations were at wavelength 400 or 375 nm so the lowest energy states involving excitation in the intramolecular charge-transfer band were excited but for ANA-1 and ANA-2 the high-energy states were also excited. Here, we focus on the emission in the red and orange-red regions that correspond to the emission from the lowest-energy band. In this energy region, the emission curves display single-exponential decay. Two of

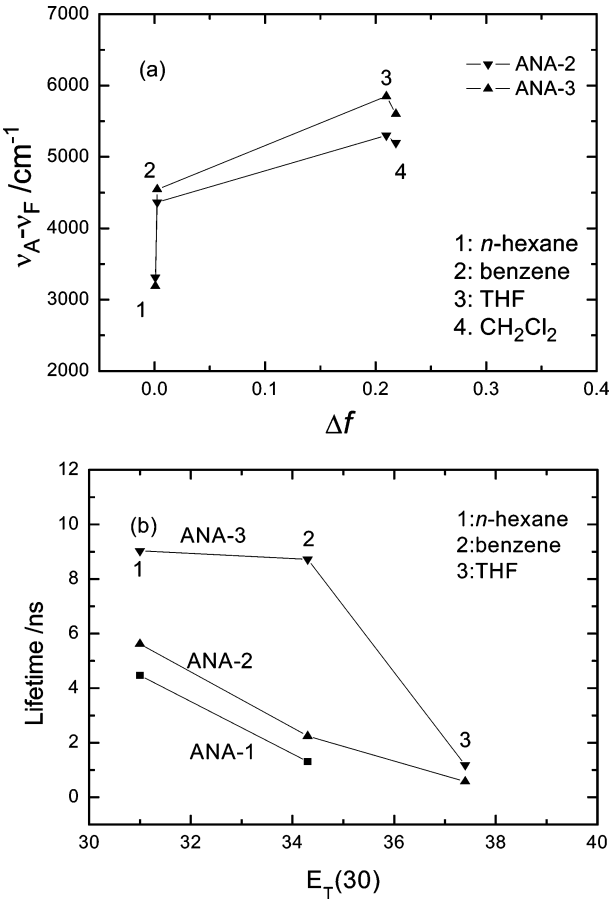

Figure 3. (a) Plots of the spectral shift of ANA-2 and ANA-3 vs Δf. (b) Plots of measured emission lifetime of ANA-1−3 vs $E_T(30)$.

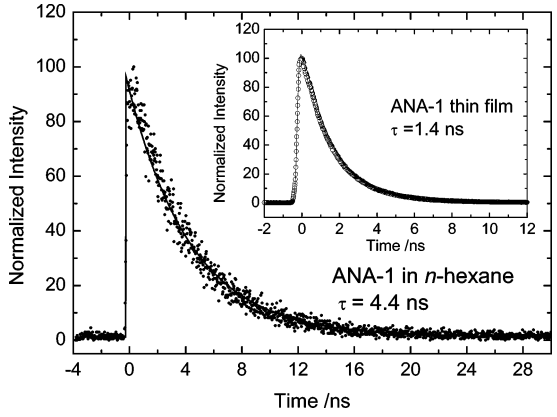

Figure 4. Fluorescence decay of ANA-1 in *n*-hexane solution and in film as the insert monitored at 580 nm and the best-fit single-exponential function. The excitation wavelength is 375 nm.

those curves are displayed in Figure 4. The results of these measurements on the emission of the state and on diluted and concentrated solutions are summarized in Table 2. The measured lifetime decreases with increase in solvent polarity; for instance, ANA-3 has a lifetime of ~8.5 ns in hexane and 1.1 ns in THF. This is further clearly shown in the plot of lifetime vs $E_T(30)$ in Figure 3b; $E_T(30)$ is another commonly used parameter denoting the polarity of a solvent.[20] These data indicate that the excited molecules are quenched efficiently by polar solvents and the quenching should be due to the dipole−dipole interaction between solvent and solute.

In film the measured lifetime is comparable to that in benzene but the emission wavelengths are consistently more red-shifted. As shown in Table 2, increase in the concentration of an ANA derivative leads to decrease of ϕ_f because of self-quenching, but the lifetime in most cases remains surprisingly long and becomes consistently longer as the monitored wavelength moves toward the longer region. These results imply the formation of a small amount of aggregates, which show relatively long lifetime of the excitons in concentrated solution.

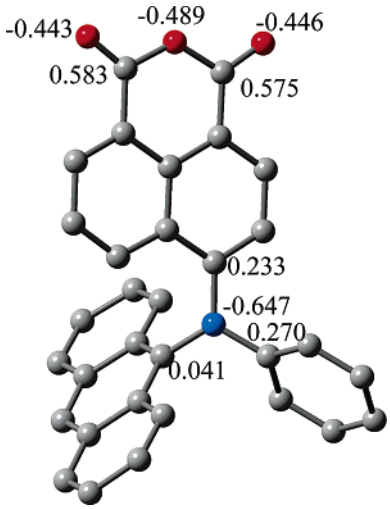

Figure 5. Optimized structures for ANA-2 with charges listed on oxygen and carbon atoms of the anhydride moiety and on nitrogen and three carbon atoms nearby based on method B3LYP/6-31G*. On the anhydride moiety, the calculated bond distances of C−O (carbonyl) are 1.207 and 1.207 Å and those of C−O (ethereal) are 1.385 and 1.392 Å.

Based on the fluorescence quantum yield for the most diluted concentration and the measured lifetime τ, we obtained the radiative rate constant k_{rad} of ANA-1−3 in *n*-hexane to be 3.0×10^7, 5.6×10^7, and 4.0×10^7 s^{-1}, respectively, using the equations $\phi_f = k_{rad}/(k_{rad} + k_{nonrad})$ and $1/\tau = (k_{rad} + k_{nonrad})$, where k_{nonrad} denotes the rate constant for the nonradiative process.

Quantum Chemical Calculations. Quantum chemical calculations based on density functional theory (DFT)[21] are performed in order to understand the energy levels and to explain the transitions of observed absorption and emission spectra of the ANA derivatives, but only on ANA-2 because of the similarity of these three molecules. The optimal geometry of the ground state for ANA-2 using method B3LYP at basis set 6-31G* is obtained and is shown in Figure 5. Vibrational frequencies were calculated to ensure no imaginary frequency existing for this structure. As shown in the figure, the three aromatic planes are nearly perpendicular to each other and the anhydride moiety has a planar geometry. From the calculated charge distributions, the center nitrogen atom carries a negative partial charge and the carbon atoms bonded to it with positive partial charge, yielding small net dipole from this part. On the anhydride moiety, three oxygen atoms are with negative partial charge and the carbons are with the opposite charge resulting in a dipole of 9.7 D (B3LYP/6-31G*). Time-dependent DFT (TD-DFT) calculation yields the first vertical transition S_1-S_0 of ANA-2, a HOMO to LUMO excitation at wavelength 486 nm with an oscillator strength of 0.1045. Based on the one-electron LUMO and HOMO characteristics, this transition involves the π electron on the nitrogen atom and anthracenyl plane to the π^* orbital in the anhydride moiety. The second vertical transition is calculated to be 443 nm and is predominantly a HOMO to LUMO+1 transition. LUMO+1 is a π^* molecular orbital mainly in the anthracenyl group. The isodensity surface plots of HOMO, LUMO, and LUMO+1 are shown

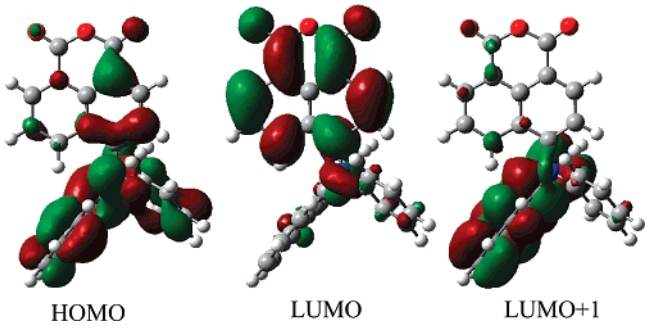

Figure 6. Isodensity surface plots (isodensity value = 0.02) of the HOMO, LUMO, and LUMO+1 of ANA-2.

in Figure 6. The calculated energy for vertical excitation of the lowest energy band is about 9% lower than the experimental value of 440 nm in *n*-hexane solution.

X-ray Structures. The structures of ANA-2 and ANA-3 were determined by single-crystal X-ray diffraction. For ANA-1, it was difficult to obtain crystals with suitable sizes for X-ray analysis. The results of these X-ray analyses show that the crystals of ANA-2 and ANA-3 are orthorhombic ($Z = 8$) and monoclinic ($Z = 4$), respectively. The structural data obtained from calculation based on the DFT in general agree with those from X-ray analysis; the deviation is less than 0.01 Å. For instance, the three aromatic moieties are also nearly perpendicular to each other based on the X-ray analysis of the crystal. On the anhydride site, the bond distances of C−O (carbonyl) are 1.208 and 1.197 Å and those of C−O (ethereal) are 1.376 and 1.389 Å and the calculated values are both 1.207 Å for the carbonyl C−O and 1.385 and 1.392 Å for the ethereal C−O bonds.

The molecular structures of these two molecules, ANA-2 and ANA-3 in crystals, show that the three substituted aromatic rings on the central nitrogen atom are nearly perpendicular to each other, but the nitrogen atom and the three attached carbons are practically coplanar. This spatial arrangement in the molecule is attributed to the mutual repulsion between the bulky substituents on the nitrogen. The molecular interactions (face-to-face packing)[22] between the molecules in ANA-3 crystal are as shown in Figure 7a. Two types of intermolecular interactions are observed, one between the anhydride moieties of molecules A and B in Figure 7, with the shortest interaction distance of 3.63 Å. These anhydride planes are arranged nearly antiparallel with a bisecting angle of 2.7°. An interaction is between the oxygen of one molecule and a carbon of the other. The second interaction is between the anhydride moiety of molecule B and the naphthalene moiety of molecule C, which are at a bisecting angle of 42°. The shortest distance between the two moieties is 3.69 Å with an interaction between the carbons of the two rings. No hydrogen bonding is observed in the ANA-3 crystal.

In contrast to ANA-3, the packing of ANA-2 in crystal is more complicated (see Figure 7b). The crystal has two sets of nonequivalent molecules in the unit cell. In addition to the hydrogen bonding, ANA-2 shows $\pi-\pi$ interactions between the carbon−carbon and oxygen−carbon of adjacent rings. Four types of interactions are observed between a set of four molecules in the unit cell forming a stack. Two molecules in the set show hydrogen bonding while the other two do not. The molecules with hydrogen bonding also show oxygen−carbon interaction at the adjacent anhydride moieties, with the shortest distances of 3.23 Å for one set and 3.29 Å for the other set and arranged at a bisecting angle of 3.8°. The two molecules with no hydrogen bonding show carbon−carbon interactions between the two adjacent anhydride moieties, with a shortest interaction

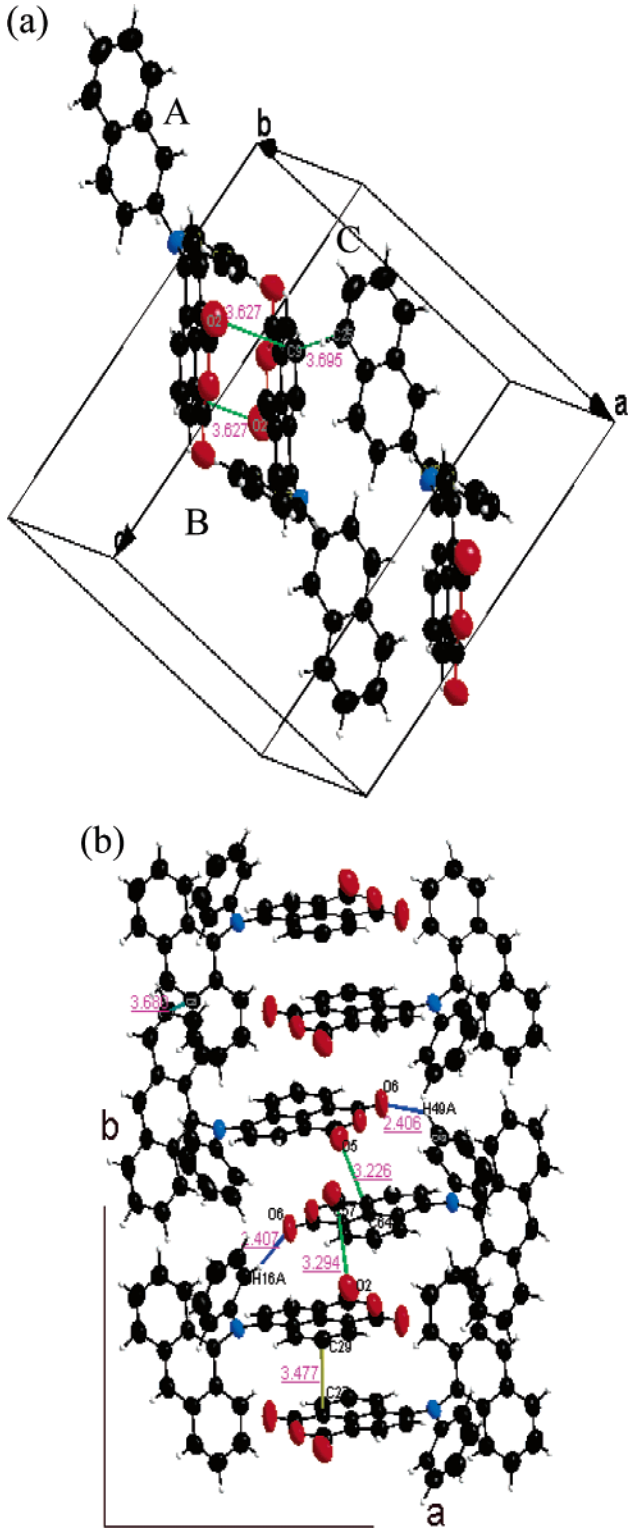

Figure 7. (a) Intermolecular interactions of ANA-3 molecules in crystals showing the antiparallel interaction of two anhydride planes and the interaction of a naphthalene and an anhydride plane. (b) Intermolecular interactions and hydrogen bonding in ANA-2 crystal projected along the *c*-axis.

distance of 3.48 Å. In this case, the two anhydride moieties are almost parallel to each other with a bisecting angle of 0.7°. In addition, a carbon−carbon interaction at 3.68 Å between the two adjacent anthracene moieties is also observed as shown in Figure 7b.

Fabrication and Performance of OLED Devices. The strong red emissive property of ANA derivatives in thin films

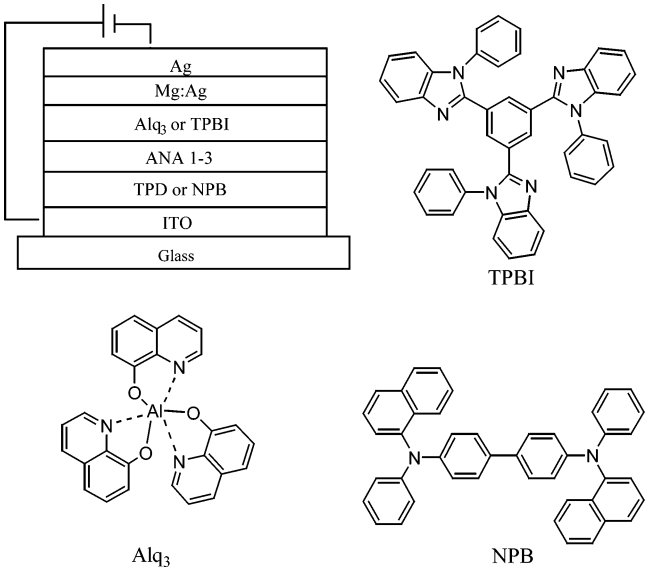

Figure 8. Electroluminescent device configuration and molecular structures of the materials used.

makes them promising candidates as red-emitting EL materials. Based on the energy-level alignment, we constructed three-layer EL devices in which the ANA derivative was used as the emitter between the hole and electron transporting layers. The general device configuration is shown in Figure 8. Alq_3 (tris[8-hydroxyquinoline]aluminum) or TPBI (1,2,3-tris[*N*-phenyl benzimidazol-2-yl]-benzene) was chosen as the electron transporter and NPB (4,4′-bis[1- naphthylphenylamino]-1,1′-biphenyl) as the hole transporter in these devices. Devices **A**−**E** were thus fabricated. Important EL data of these devices are listed in Table 3, while EL spectra of devices **A**−**E** are depicted in Figure 2c. As seen in the figure, device **A** (ITO/NPB/ANA-1/Alq_3/Mg:Ag/Ag) emits saturated red light at 628 nm with CIE coordinates at ($X = 0.63$, $Y = 0.36$). A low turn-on voltage of 4.0 V with maximum brightness of 4700 cd/m^2 at 14.5 V, external quantum efficiency of 0.38 at 10.5 V, and power efficiency of 0.38 lm/W were observed for this device. The external quantum efficiency of this device remains nearly constant with applied voltage and the current density (Figure 9). There is essentially no change of EL spectra and CIE coordinates of the device for an applied voltage in the range 7−12 V.

Device **B** in which TPBI serves as the hole blocking and electron transporting material consists of the layers ITO/NPB/ANA-1/TPBI/Mg:Ag/Ag. The EL data are listed in Table 3. For comparison with other devices, the EL data at 100 mA/cm^2 are also reported in parentheses in the same table. Device **B** shows EL characteristics similar to device **A**. The maximum brightness (4870 cd/m^2) is marginally better than that of device **A**; the CIE values for device **B** are located at ($X = 0.63$, $Y = 0.37$) and do not change with applied voltage.

Devices **C** and **D** were constructed based on ANA-2 as the emitter, NPB as the hole transporter, and TPBI or Alq_3 as the electron transporter. Both devices give orange emission at 602 and 603 nm, respectively. The CIE coordinates appear at ($X = 0.58$, $Y = 0.42$) for device **C** and at ($X = 0.57$, $Y = 0.43$) for **D**. The other data are listed in Table 3. In device **E**, ANA-3 served as the emitting layer, whereas NPB and TPBI served as hole- and electron-transporting layers, respectively. The maximum brightness for device **E** is 7482 cd/m^2 at voltage 12.3 V, whereas the external quantum, current, and power efficiency are 0.424%, 0.731cd/m^2, and 0.364 lm/W, respectively. The EL spectrum shows an emission maximum at 619 nm and CIE values of ($X = 0.62$, $Y = 0.38$). The brightness and external quantum efficiency of device **E** are better than the corresponding values for the devices based on ANA-1 and ANA-2 as emitters.

3. Discussion

In nonpolar solvents such as *n*-hexane, ANAs exist as monomers and have similar properties as an isolated molecule. From DFT calculations, it is observed that the lower energy absorption centered around 450 nm has charge-transfer character from the arylamino group to the anhydride moiety. Owing to their large polarity change, as the polarity of the solvent increases from hexane to dichloromethane, we observe a red shift in the emission maxima of the molecule. This can be employed to explain the red-shifted emission of ANA molecules in film where the neighboring polar ANA molecules interact with the excited ANA state lowering the energy level of the excited state. Bulovic et al.[7c] reported a method for tuning the electroluminescence spectrum of DCM2-based devices by adjusting the concentration of DCM2 in the organic host. A high concentration of DCM2 led to longer emission wavelength due to the solid-state solvation effect, a dipole−dipole interaction of excited DCM2 molecules with DCM2 molecules in the solid state. Similarly these ANA derivatives can be used for tuning the wavelength of electroluminescence.

A change in the ability of a solvent to form hydrogen bonds can affect the nature of the lowest singlet state. This was observed in methanol solution. A larger blue shift ($\approx$72 nm) for ANA-1 and ANA-3 and a shift of $>$40 nm were observed for ANA-2. According to the calculated HOMO and LUMO as shown in Figure 6, formation of hydrogen bonding is expected to stabilize the HOMO and destabilize the LUMO energy by bonding to the amino group where the negative charge is the highest in the molecule (see Figure 5). This causes a hypsochromic shift in absorption. In methanol we observed ANAs to be almost nonfluorescent because hydrogen bonding presumably enhances nonradiative processes.[23] Molecule ANA-2 showing consistently blue shifts in absorption and emission spectra compared with ANA-1 and ANA-3 can be explained to be the nearly perpendicular dihedral angles between the anthracenyl group and the anhydride group for ANA-2 from the X-ray structure. This geometry hampers π-electron conjugation between the anthracenyl and the anhydride groups and possibly results in blue shifts in the observed spectra.

TABLE 3: Performance of the Electroluminescent Devices Based on ANA Derivatives[a]

device[b]	V_t	η (%, V)	cd/m^2, V	cd/A, V	lm/W, V	CIE, (x, y)	λ_{max}(nm)
A	4.0	0.381, 10.5 (0.372)	4700, 14.5 (476)	0.521, 10.0 (0.509)	0.380, 3.5 (0.178)	(0.63, 0.36)	628
B	4.0	0.379, 10.0 (0.376)	4870, 15.0 (645)	0.545, 10.5 (0.540)	0.355, 3.5 (0.178)	(0.63, 0.37)	626
C	3.0	0.198, 8.5 (0.172)	4470, 11.5 (381)	0.454, 8.5 (0.393)	0.212, 5.5 (0.206)	(0.58, 0.42)	602
D	4.0	0.177, 10.0 (0.162)	3530, 13.4 (361)	0.409, 10.0 (0.373)	0.268, 3.5 (0.147)	(0.57, 0.43)	603
E	3.0	0.424, 8.0 (0.393)	7480, 12.3 (791)	0.731, 8.0 (0.677)	0.364, 5.5 (0.354)	(0.62, 0.38)	619

[a] The external quantum efficiency, brightness, current efficiency, and power efficiency recorded are the maximum values for the device, and those in the parentheses were taken at a current density of 100 mA/cm^2. [b] Devices with thickness listed in the parentheses in units of nm: (**A**) NPB (50)/ANA-1 (50)/Alq_3 (50); (**B**) NPB (40)/ANA-1 (40)/TPBI (40); (**C**) NPB (40)/ANA-2 (40)/TPBI (40); (**D**) NPB (40)/ANA-2 (40)/Alq_3 (40); (**E**) NPB (40)/ANA-3 (40)/TPBI (40).

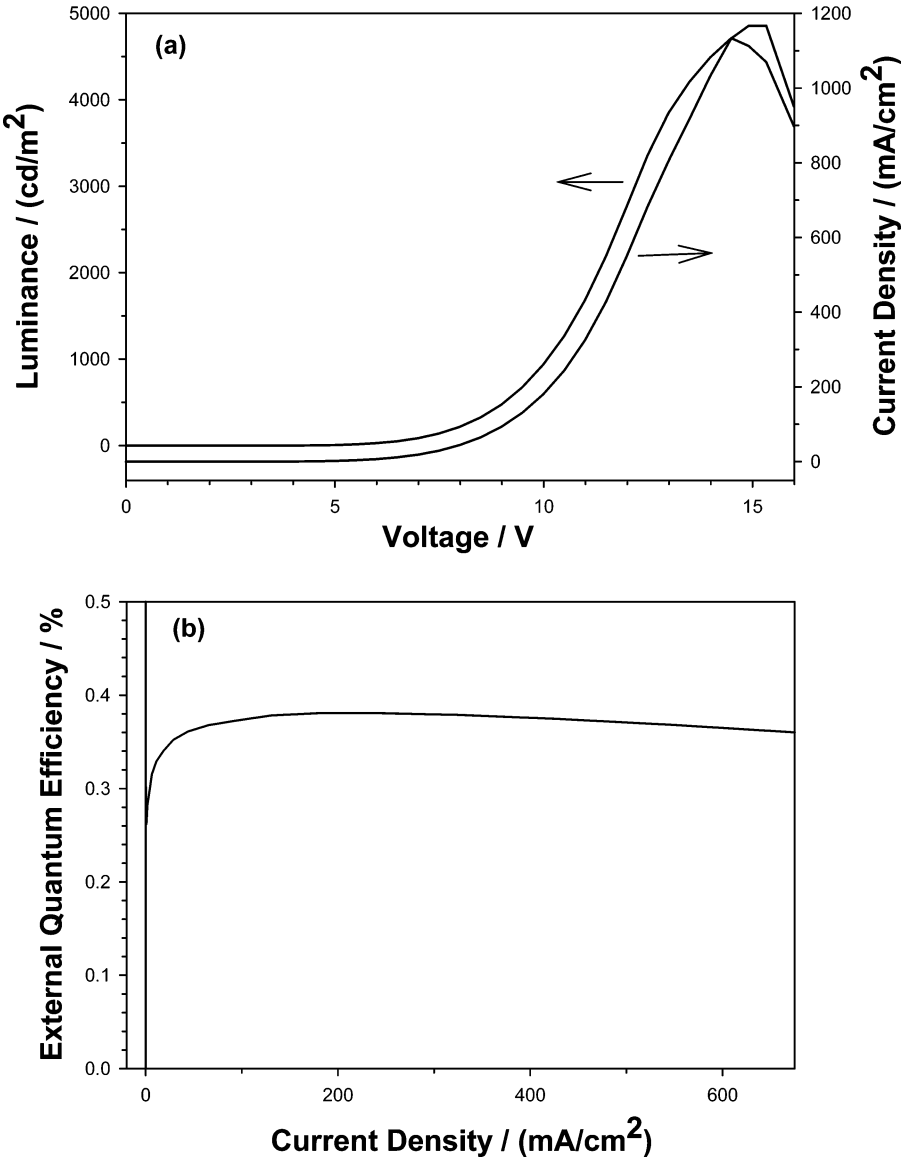

Figure 9. (a) Current density−voltage−luminance ($I-V-L$) characteristics of device **A** [ITO/NPB (50 nm)/ANA-1 (50 nm)/Alq_3 (50 nm)/Mg:Ag]. (b) External quantum efficiency vs current density plot for device **A**.

For these ANA molecules, the degree of red shift of the emission maximum for films is comparable to that in THF, but the measured emission lifetimes for films are comparable to those in benzene. In addition, the brightness and external quantum efficiency of EL devices based on these ANA emitters remain quite good indicating that there is no significant quenching by the nearby molecules. At high concentrations of the ANA molecules in solutions, we observed no lifetime shortened. Furthermore, the red part of the emission band displays longer lifetimes. This is attributed to the formation of aggregates in the concentrated solution as well as in film. The structure of the aggregates can be correlated to the X-ray data in the crystalline solid state.[24] In film the actual structures of these compounds are expected to exhibit similar stacking as those in crystal, but with less degree of crystalline order. Aggregation is expected to further bathochromically shift the emission in addition to the polar environment of the host.

In summary, we have successfully synthesized the organic compounds consisting of a 4-amino-1,8-naphthalic anhydride group and employed these compounds as orange and red emitters in organic EL devices. These compounds served as direct emitters instead of dopants typical in most red light emitting EL devices. A simple three-layer red-emitting device with good luminous efficiency and color purity was achieved by using ANA-1 as the host emitter. The EL and PL spectra in thin films that show drastic red shift relative to the corresponding values in hexane solution originate from the stabilization by the polar environment and the $\pi-\pi$ stacking. Based on the emission lifetime data, aggregation in film and EL devices further accounts for the red shifts of the emission. The high sensitivity of the emission wavelength and intensity of these molecules with environment also find their potential application as solvatochromic luminescent probes.

4. Experimental Section

General Procedure for Synthesis of ANA Derivatives (1−3). To a two-necked flask under nitrogen were added 4-bromo-1,8-naphthalic anhydride (1 mmol), a secondary amine (1.2 mmol), $Pd(OAc)_2$ (0.020 mmol), tri-*tert*-butyl phosphine (0.040−0.050 mmol), and sodium *tert*-butoxide (1.5 mmol). Toluene (3 mL) was then added to the flask via a syringe. The resulting mixture was stirred for 4−6 h at 120 °C. After cooling, to the mixture was added water (3 mL) and then ethyl acetate

(20 mL). The organic layer was separated from the aqueous layer, washed successively with water and brine solution, and dried over anhydrous magnesium sulfate. Evaporation of the solvent under reduced pressure afforded the crude solid. Purification on a silica gel column using a dichloromethane/hexane mixture as the eluent gave the desired pure product. Yields and important spectral data of these products appear below.

4-(Phenyl pyren-1-yl)amino-1,8-naphthalic Anhydride (ANA-1). Yield: 70%. ^{1}H NMR (400 MHz, $CDCl_3$, TMS): δ 8.53 (dd, J = 0.8, 8.4 Hz, 1H), 8.39 (d, J = 8.4 Hz 1H), 8.32 (dd, J = 0.8, 8.4 Hz, 1H), 8.22 (d, J = 7.6 Hz, 1H), 8.18−8.03 (m, 6H), 7.95 (d, J = 9.2 Hz, 1H), 7.69 (d, J = 8.0 Hz, 1H), 7.43 (dd, J = 7.2, 15.6 Hz, 1H), 7.24−7.22 (m, 4H), 7.10 (t, J = 7.2, 14.8 Hz, 1H), 6.89 (brs, 1H). UV−vis λ_{max} (CH_2Cl_2): 245, 307, 362, 467 nm. HRMS: calcd for $C_{34}H_{19}NO_3$, 489.1365; found, 489.1346.

4-(Phenyl anthracen-9-yl)amino-1,8-naphthalic Anhydride (ANA-2). Yield: 73%. ^{1}H NMR (400 MHz, $CDCl_3$, TMS): δ 8.60 (d, J = 8.0 Hz, 2H), 8.48 (d, J = 8.4 Hz, 1H), 8.25 (d, J = 8.4 Hz, 1H), 8.10 (d, J = 8.4, Hz, 2H), 8.05 (d, J = 8.8 Hz, 2H), 7.56 (dd, J = 7,4, 16.0 Hz, 1H), 7.46 (t, J = 6.4, 14.8 Hz, 2H), 7.38−7.34 (m, 2H), 7.16 (t, J = 8.0, 16.0 Hz, 1H), 7.02−6.95 (m, 2H), 6.85 (dd, J = 0.8. 8.4 Hz, 2H). UV−vis λ_{max} (CH_2Cl_2): 249, 306, 406, 461 nm. HRMS: calcd for $C_{32}H_{19}NO_3$, 465.1365; found, 465.1352.

4-(Phenyl-2-naphthyl)amino-1,8-naphthalic Anhydride (ANA-3). Yield: 75%. ^{1}H NMR (400 MHz, $CDCl_3$, TMS): δ 8.52−8.48 (m, 2H), 8.24 (dd, J = 0.8, 8.4 Hz 1H), 7.79−7.76 (m, 2H), 7.56−7.54 (m, 1H), 7.49−7.45 (m, 1H), 7.42−7.38 (m, 3H), 7.32−7.28 (m, 3H), 7.24−7.22 (m, 1H), 7.16−7.12 (m, 1H), 7.06 (dd, J = 1.2, 8.4 Hz 1H). UV−vis λ_{max} (CH_2Cl_2): 240, 274, 306, 469 nm. HRMS: calcd for $C_{28}H_{17}NO_3$, 415.1209; found, 415.1210.

Measurement of Physical Properties and Device Fabrication. The glass transition temperature (T_g) and melting points were obtained from differential scanning calorimetry (DSC) measurement, performed on a Seiko SII-EXSTAR 6000-dsc-6200 differential scanning calorimeter. UV−vis absorption spectra were recorded using a Hitachi U-300 spectrophotometer, while PL and EL spectra were measured on a Hitachi F-4050. The ANA derivatives are dissolved in benzene, *n*-hexane, methanol, and THF with various concentrations in order to observe the change of photochemical properties. The HOMO levels are calculated from the oxidation−reduction potential obtained from the cyclic voltammetry (CV) curves. Cyclic voltammetric experiments were carried out using a CHI 600A electrochemical analyzer. The LUMO levels are estimated based on the HOMO energy level and the lowest-energy absorption edge of the UV−vis absorption spectrum.[25]

The EL devices based on ANA derivatives were made by vacuum deposition of the materials at the deposition rate of 1−2 Å s^{-1}. The cathode was then capped with Ag metal (100 nm) by evaporation of Ag at a rate of 3 Å s^{-1}. The electron-transporting materials used are Alq_3 (tris[8-hydroxyquinoline]-aluminum) or TPBI (1,2,3-tris[*N*-phenylbenzimidazol-2-yl]-benzene), and the hole-transporting materials are NPB (4,4′-bis[1-naphthylphenylamino]-1,1′-biphenyl) or TPD (4,4′-bis[3-tolylphenylamino]-1,1′-biphenyl), with the thickness of 40 nm, respectively. The effective area of the emitting diode is 9.00 mm^2. Current, voltage, and light intensity measurements were made simultaneously using a Keithley 2400 source meter and a Newport 1835-C optical meter.

Fluorescence Lifetime and Quantum Yield Measurements. For picosecond lifetime measurements, we used time-correlated single photon counting (TCSPC) implemented with a diode laser (PicoQuant, PDL-800-B, pulse width of 50 ps, repetition rate reduced to 3 MHz) at wavelength 375 nm, or output of the second harmonic generation of the fundamental beam from a Ti-sapphire femtosecond laser (Spectra Physics Maitai, pulse width of 100 fs) at 400 nm. The output of the femtosecond laser was modulated by a pulse selector (Spectra Physics 3980) to reduce the repetition rate to 1 MHz. The overall temporal resolution (≈120−130 ps) is limited by combination of the temporal response of MCP-PMT (Hamamatsu R3809U-50), time-to-amplitude converter (EG&G ORTEC), and pulse width of the diode laser. Emission was detected by the PMT after a pair of collection lenses and a suitable interference filter.

Absolute quantum yields for emission were measured at room temperature with fluorescein (in 0.1 M NaOH, quantum yield = 0.93) as the standard. These yields for ANA-1−3 in hexane, benzene, and THF are listed in Table 2.

Computational Methods. Quantum chemical calculations based on the DFT were performed to obtain the optimized geometries. Method B3LYP at basis set 6-31G* was employed for ANA-2 to achieve reliable results. Time-dependent DFT based on the optimized geometry of B3LYP/6-31G* is used to obtain the vertical transitions and their oscillator strengths on ANA-2. All calculations were performed with the Gaussian 98 program (version A.9)[26] on a workstation or on personal computers.

Acknowledgment. The authors are grateful to Professor Yu-Tai Tao for assistance with experiments and valuable suggestions and to the Ministry of Education (89-FA04-AA) and the National Science Council, Taiwan, for financial support.

Supporting Information Available: The crystal data for ANA-2 and ANA-3 and the structural information for ANA-2 using B3LYP/6-31G. This material is available free of charge via the Internet at http://pubs.acs.org.

References and Notes

(1) (a) Tang, C. W.; VanSlyke, S. A. *Appl. Phys. Lett*. **1987**, *51*, 913. (b) Hung, L. S.; Chen, C. H. *Mater. Sci. Eng. R* **2002**, *39*, 143 and references therein.

(2) Baldo, M. A.; Lamansky, S.; Burrows, P. E.; Thomson, M. E.; Forest, S. R. *Appl. Phys. Lett.* **1999**, *75*, 4.

(3) (a) Adachi, C.; Tsutsui, T.; Saito, S. *Appl. Phys. Lett.* **1990**, *57*, 531. (b) Kido, J.; Iizumi, Y. *Chem. Lett.* **1997**, 693.

(4) (a) Hosokawa, C.; Tokailin, H.; Higashi, H.; Kusumoto, T. *J. Appl. Phys.* **1995**, *78*, 5831. (b) Yang, Y.; Pei, Q.; Hegger, A. J. *J. Appl. Phys.* **1996**, *79*, 934.

(5) Chen, C. H.; Tang, C. W. *Appl. Phys. Lett.* **2001**, *79*, 3711.

(6) (a) Shih, H.-T.; Lin, C.-H.; Shih, H.-S.; Cheng, H.-C. *Adv. Mater.* **2002**, *14*, 1409. (b) Kim, Y.-H.; Shin, D. C.; Kim, S.-H.; Ko, C.-H.; Yu, H.-S.; Chae, Y.-S.; Kwon, S. K. *Adv. Mater*. **2001**, *13*, 1690. (c) Shi, J.; Tang, C. W. *Appl. Phys. Lett.* **2002**, *80*, 3201.

(7) (a) Tang, C. W.; Van Slyke, S. A.; Chen, C. H. *J. Appl. Phys.* **1989**, *65*, 3610. (b) Zhang, X. H.; Chen, B. J.; Lin, X. Q.; Wong, O. Y.; Lee, C. S.; Kwong, H. L.; Lee, S. T.; Wu, S. K. *Chem. Mater.* **2001**, *13*, 1565. (c) Bulovic, V.; Deshpande, R.; Thompson, M. E.; Forrest, S. R. *Chem. Phys. Lett.* **1999**, *308*, 317.

(8) Chen, C. H.; Tang, C. W.; Shi, J.; Klubek, K. P. *Thin Solid Films* **2000**, *363*, 327.

(9) Mal'tsev, E. I.; Lypenko, D. A.; Shapiro, B. I.; Brusentseva, M. A.; Milburn, G. H. W.; Wright, J.; Hendriksen, A.; Berendyaev, V. I.; Kotov, B. V.; Vannikov, A. V. *Appl. Phys. Lett.* **1999**, *75*, 1896.

(10) Era, M.; Adachi, C.; Tsutsui, T.; Saito, S. *Chem. Phys. Lett.* **1991**, *178*, 488.

(11) (a) Sakakibara, Y.; Okutsu, S.; Enokida, T.; Tani, T. *Appl. Phys. Lett.* **1999**, *74*, 2587. (b) Burrows, P. E.; Forrest, S. R.; Sibley, S. P.; Thompson, M. E. *Appl. Phys. Lett.* **1996**, *69*, 2959.

(12) Baldo, M. A.; O'Brien, D. F.; You, Y.; Shoustikov, A.; Sibley, S.; Thompson, M. E.; Forrest, S. R. *Nature* (*London*) **1998**, *395*, 151.

(13) (a) Huang, L.; Wang, K.-Z.; Huang, C.-H.; Li, F.-Y.; Huang, Y.-Y. *J. Mater. Chem.* **2001**, *11*, 790. (b) Heil, H.; Steiger, J.; Schmechel, R.;

von Seggern, H. *J. Appl. Phys.* **2001**, *90*, 5357. (c) Sun, P.-P.; Duan, J.-P.; Shih, H.-T.; Cheng, C.-H. *Appl. Phys. Lett.* **2002**, *81*, 792.

(14) (a) Adachi, C.; Baldo, M. A.; Forrest, S. R.; Lamansky, S.; Thompson, M. E.; Kwon, R. C. *Appl. Phys. Lett.* **2001**, *78*, 1622. (b) Lamansky, S.; Djurovich, P.; Murphy, D.; Abdel-Razzaq, F.; Lee, H.-E.; Adachi, C.; Burrows, P. E.; Forrest, S. R.; Thompson, M. E. *J. Am. Chem. Soc.* **2001**, *123*, 4304.

(15) (a) Thomas, K. R. J.; Lin, J. T.; Tao, Y.-T.; Chuen, C.-H. *Adv. Mater.* **2002**, *14*, 822. (b) Kim, J. H.; Lee, H. *Chem. Mater.* **2002**, *14*, 2270. (c) Ma, C.; Zhang, B.; Liang, Z.; Xie, P.; Wang, X.; Zhang, B.; Cao, Y.; Jiang, X.; Zhang, Z. *J. Mater. Chem.* **2002**, *12*, 1671. (d) Wu, W. C.; Yeh, H. C.; Chen, L. H.; Chen, C. T. *Adv. Mater.* **2002**, *14*, 1072.

(16) Yamamoto, T.; Nishiyama, M.; Koie, Y. *Tetrahedron Lett.* **1998**, *39*, 2367.

(17) Su, J.; Xu, T.; Chen, K.; Tian, H. *Synth. Met.* **1997**, *91*, 249.

(18) (a) Birks, J. B. *Rep. Prog. Phys.* **1975**, *38*, 903. (b) Winnik, F. M. *Chem. Rev.* **1993**, *93*, 587 and references therein. (c) Jones, G., II; Vullev, V. I. *J. Phys. Chem. A* **2001**, *105*, 6402. (d) Hayashi, T.; Mataga, N.; Sakata, Y.; Misumi, S.; Morita, M.; Tanaka, J. *J. Am. Chem. Soc.* **1976**, *98*, 5910 and references therein.

(19) Lippert, E. Z. *Naturforsch.* **1955**, *10a*, 541.

(20) Reichardt, C. *Solvents and Solvent Effects in Organic Chemistry*, 2nd ed.; VCH: Weinheim, 1988.

(21) Bickelhaupt, F. M.; Baerends, E. J. *Rev. Comput. Chem.* **2000**, *15*, 1 and references therein.

(22) Gulyani, A.; Gopalan, R. S.; Kulkarni, G. U.; Bhattacharya, S. *J. Mol. Struct.* **2002**, *616*, 103.

(23) Saroja, G.; Soujanya, T.; Ramachandram, B.; Samanta, A. *J. Fluoresc.* **1998**, *8*, 405.

(24) (a) Lewis, F. D.; Yang, J.-S.; Stern, C. L. *J. Am. Chem. Soc.* **1996**, *118*, 2772−2773. (b) Lewis, F. D.; Yang, J.-S. *J. Phys. Chem. B* **1997**, *101*, 1775. (c) Singh, A. K.; Krishna, T. S. R. *J. Phys. Chem. A* **1997**, *101*, 3066. (d) Brinkmann, M.; Gadret, G.; Muccini, M.; Taliani, C.; Masciocchi, N.; Sironi, A. *J. Am. Chem. Soc.* **2000**, *122*, 5147.

(25) Janietz, S.; Bradley, D. D. C.; Grell, M.; Giebeler, C.; Inbasekaran, M.; Woo, E. P. *Appl. Phys. Lett.* **1998**, *73*, 2453.

(26) Frisch, M. J.; Trucks, G. W.; Schlegel, H. B.; Scuseria, G. E.; Robb, M. A.; Cheeseman, J. R.; Zakrzewski, V. G.; Montgomery, J. A., Jr.; Stratmann, R. E.; Burant, J. C.; Dapprich, S.; Millam, J. M.; Daniels, A. D.; Kudin, K. N.; Strain, M. C.; Farkas, O.; Tomasi, J.; Barone, V.; Cossi, M.; Cammi, R.; Mennucci, B.; Pomelli, C.; Adamo, C.; Clifford, S.; Ochterski, J.; Petersson, G. A.; Ayala, P. Y.; Cui, Q.; Morokuma, K.; Malick, D. K.; Rabuck, A. D.; Raghavachari, K.; Foresman, J. B.; Cioslowski, J.; Ortiz, J. V.; Stefanov, B. B.; Liu, G.; Liashenko, A.; Piskorz, P.; Komaromi, I.; Gomperts, R.; Martin, R. L.; Fox, D. J.; Keith, T.; Al-Laham, M. A.; Peng, C. Y.; Nanayakkara, A.; Gonzalez, C.; Challacombe, M.; Gill, P. M. W.; Johnson, B. G.; Chen, W.; Wong, M. W.; Andres, J. L.; Head-Gordon, M.; Replogle, E. S.; Pople, J. A. *Gaussian 98*, revision A.9; Gaussian, Inc.: Pittsburgh, PA, 1998.